

Classical aspects of ultracold atom wavepacket motion through microstructured waveguide bends

M.W.J. Bromley* and B.D. Esry†

Department of Physics, Kansas State University, Manhattan, KS 66506 USA

(Dated: May 9, 2019)

Abstract

The properties of low-density, low-energy matter wavepackets propagating through waveguide bends are investigated. Time-dependent quantum mechanical calculations using simple harmonic oscillator confining potentials are performed for a range of parameters close to those accessible by recent “atom chip”-based experiments. We compare classical calculations based on Ehrenfest’s theorem to these results to determine whether classical mechanics can predict the amount of transverse excitation as measured by the transverse heating. The present results thus elucidate some of the limits for which matter wave propagation through microstructures can be reliably considered using classical particle motion.

PACS numbers: 03.75.Be 03.75.Kk 45.50.Dd 02.70.Bf

*Electronic address: bromley@phys.ksu.edu

†Electronic address: esry@phys.ksu.edu

I. INTRODUCTION

Recent experimental progress in atomic physics includes the success of magnetic microtraps [1] — the so-called “atom chips” [2] — where combinations of magnetic fields and wires layed on silica substrates have made possible atom traps, guides and devices all above a single chip [3, 4].

The strong magnetic field gradients created by microtraps have already proven their versatility. Bose-Einstein condensates (BECs) have been created above microchip surfaces using evaporation [5, 6, 7, 8] and also by using the surface itself as a hot atom knife to condense a cloud of atoms [9, 10]. These achievements are significant since a BEC is the most likely source to feed atom-optical devices as they provide a large number of coherent atoms. In fact, the controlled propagation of BECs through atom chip waveguides has already been demonstrated [11, 12, 13], and some sources of decoherence have been identified [8, 14, 15].

Non-linear interactions in atom optics can be useful [16], but recent theoretical investigations have demonstrated that such effects can potentially degrade atom optical device performance [17, 18, 19, 20]. Furthermore, despite the possibility of using multi-moded matter waves [21, 22, 23], the low-density regime with single-mode propagation is expected to make atom optical devices much simpler and easier to operate. With this in mind, previous theoretical investigations of the low-velocity, low-density matter wave limit have delineated the conditions for single-moded wave propagation through microstructures [24, 25, 26, 27].

In the present paper, we further explore the conditions under which propagation is single-moded, and the extent to which classical mechanics can predict the transverse excitation. Specifically, the time-dependent scattering of a wavepacket through a circular bend is investigated, neglecting atom-atom interactions. The curved waveguide is a fundamental system that forms the basis for many geometries already experimentally realised, such as multiple circular bends [28], storage rings [29], spiral guides [30] and stadium shaped traps [31]. Note that these experiments all used atoms with relatively high energies, not ground mode atoms, and thus the atomic motion was modelled using Monte Carlo ensembles of classical particles [28, 29, 30].

The time-dependent quantum mechanical calculations explore the low-energy, tight bend limit, as well as regimes not easily accessible with our previous time-independent calculations of the circular bend system [26]: large radii bends and small de Broglie wavelengths. Classical

particle calculations using Ehrenfest’s theorem are performed alongside such wavepacket calculations to highlight the connections between the two pictures of atom propagation:

$$\begin{aligned} \frac{d\langle x \rangle}{dt} &= \frac{\langle p_x \rangle}{m}, \\ \frac{d\langle p_x \rangle}{dt} &= - \left\langle \frac{\partial V(x, y, z)}{\partial x} \right\rangle \\ &\approx - \frac{\partial V(\langle x \rangle, \langle y \rangle, \langle z \rangle)}{\partial \langle x \rangle}. \end{aligned} \tag{1}$$

That is, the center-of-mass motion of a wavepacket can be approximated by a *single* trajectory of a classical particle, which we call the Ehrenfest trajectory. While Ehrenfest’s theorem is generally exact for simple harmonic oscillators (SHOs), our bend is only an SHO in the transverse direction. So, the question asked here is how well the approximation introduced in Eq. (1) reproduces the exact Ehrenfest’s theorem, and thus the quantum mechanical results. We are not, however, testing the use of Monte Carlo ensembles of classical particles to approximate the quantum observables. Jääskeläinen and Stenholm [32], for example, have explored such an approach and found excellent agreement for the “transverse cooling” of a wavepacket exiting an abruptly terminating transverse potential (when quantum reflections do not play a role).

In our calculations, remarkable agreement is seen between the “transverse heating” for the quantum wavepacket and for its Ehrenfest trajectory, when wavepacket properties such as dispersion can be neglected (in accordance with our approximation to Ehrenfest’s theorem) and where large quantum numbers are involved (in accordance with Bohr’s correspondence principle). It will also be seen that the transverse heating of the Ehrenfest trajectories and the wavepackets are in disagreement with analytic expressions obtained by Blanchard and Zozulya for high-velocity atoms and large radii bends [33]. The present results provide guidance as to when matter wave propagation through microstructures can be reliably considered using classical particle motion.

II. DETAILS OF THE CALCULATIONS

Whilst there are a variety of atom chip wire configurations both proposed and experimentally proven [4, 34], the same theoretical ansatz found in [26] was adopted here. That is, only multiple wire configurations that do not require external bias fields applied in the plane

of the microchip surface are considered [30]. The problems relating to Majorana spin-flips during propagation in the zero-field region of such geometries are ignored here, although it is noted that Luo *et.al.* [30] have proposed a rotating potential scheme to avoid these losses.

Our model reduces exactly to a 2-D geometry without losing any physics, as the out-of-plane potential remains constant through the bend in the limit where atom-atom interactions are neglected (in other words, the out-of-plane quantum number is conserved [26]). In practice, guiding potentials are quadratic near their minima, so a simple harmonic oscillator (SHO) potential is employed here:

$$V = \begin{cases} \frac{1}{2}m\omega^2(x - \rho_0)^2 & z \leq 0 , \\ \frac{1}{2}m\omega^2(\rho - \rho_0)^2 & 0 \leq \phi \leq \phi_0 , \\ \frac{1}{2}m\omega^2(x - \rho_0)^2 & z \geq 0 . \end{cases} \quad (2)$$

Configuration space has been divided into two straight leads described by Cartesian coordinates and the circular bend connecting them. The bend has radius ρ_0 and angle ϕ_0 , and is described by polar coordinates. The potential for a relatively tight ($\rho_0 = 20$), 90° bend is shown in Fig. 1.

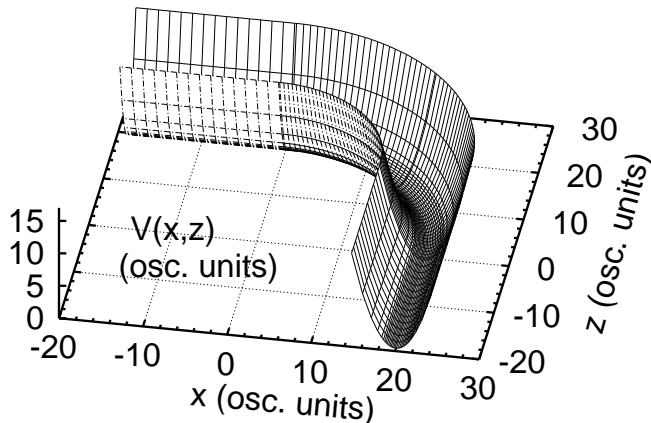


FIG. 1: Potential energy surface for a $\rho_0 = 20$, $\phi_0 = 90^\circ$ SHO-based circular bend. Both the energy and coordinates are given in oscillator units. The coordinates are those relative to the $z \leq 0$ region of Eq. (2).

Oscillator units are used throughout this paper (unless indicated otherwise), where energies are in units of $\hbar\omega$, lengths are in units of $\beta = \sqrt{\hbar/m\omega}$, and time is in units of $1/\omega$. Table

I shows some typical values for ^{87}Rb atoms trapped with a transverse oscillator frequency of $\omega = 2\pi \times 97$ Hz [12]. This combination gives $\beta \approx 1.09\mu\text{m}$. The SHO energy spectrum and associated velocity, temperature, and wavelength are also shown. These values correspond to the thresholds of propagation for each mode.

TABLE I: Conversion of oscillator units to S.I. units for ^{87}Rb atoms trapped by a transverse oscillator frequency $\omega = 2\pi \times 97$ Hz, *i.e.* an oscillator width $\beta \approx 1.09\mu\text{m}$. The energy of each SHO mode is given in oscillator units. Also given are the velocity, temperature, and wavelength corresponding to the thresholds of propagation for each mode.

n	E_{lead} (osc.)	v_z (osc.)	E_k (μK)	v_z (mm s^{-1})	λ (μm)
0	0.50	0	0	0	∞
1	1.50	$\sqrt{2}$	38.71	0.943	4.86
2	2.50	2	77.41	1.334	3.44
3	3.50	$\sqrt{6}$	116.1	1.634	2.81
4	4.50	$2\sqrt{2}$	154.8	1.887	2.43
32	32.5	8	1239	5.336	0.860

The time-propagation calculations are performed using a split-operator Crank-Nicolson method with finite differences on a non-uniform, non-Cartesian grid. The details of our implementation of the differencing are discussed in Appendix A (see also Ref. [35]), but we will outline the time propagation scheme below.

We first note that we use a hybrid (Cartesian plus polar) grid to improve the efficiency and accuracy of the calculations. A purely Cartesian grid is, in general, computationally wasteful for bends with angles other than 0° , so uniform Cartesian grids in the leads are joined with a uniform polar grid in the bend. Higher accuracy is possible by using the coordinate system best adapted to each region. The same non-uniform transverse grid is used in both the leads and the bend, with the density of grid points greatest at ρ_0 , the center of the potential valley. An example grid is shown in Fig. 2 plotted as a function of z' , which is an auxillary coordinate that measures the distance along the guide from the middle of the bend ($z' = 0$ at $\phi = \phi_0/2$). This scheme minimises the number of gridpoints required for long propagation times through arbitrary angle bends. In this transformed grid, $2N_z$ plus

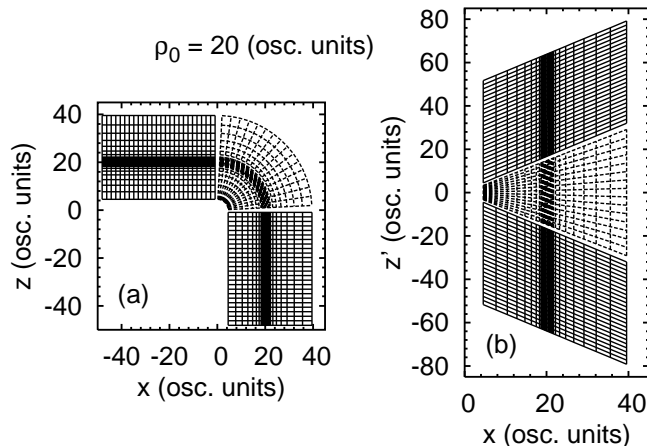


FIG. 2: Example non-Cartesian, non-uniform grid used for the Crank-Nicolson with finite-differences calculations for a $\phi_0 = 90^\circ$ circular bend with $\rho_0 = 20$. (a) shows the grid points translated to a Cartesian coordinate system. (b) shows the grid points used in the calculations: where the coordinate transverse to the direction of propagation in both the leads and bend is given by x , while z' is an auxiliary coordinate that measures the distance from the middle of the bend ($z' = 0$ at $\phi = \phi_0/2$) along an equipotential line. The grid points located within the bend are connected with the dashed lines for clarity.

N_ϕ gridpoints are along the direction of propagation, and the grid spacing δ_z and $\rho_0\delta_\phi$ are chosen to be roughly the same. The significant computational benefit of using the hybrid grid was that calculations of bends with large radii require essentially the same number of transverse grid points N_x as smaller bends. There is a small error introduced where the Cartesian and polar grids are joined since the differencing there assumes the grid lines are parallel. This error decreases with increasingly dense grids and with growing ρ_0 .

The time-dependent solution of the Schrödinger equation is

$$\Psi(x, z, t + \delta_t) = e^{-iH\delta_t}\Psi(x, z, t). \quad (3)$$

One way to evaluate the exponential operator is to write $H = T + V$ and use the standard split operator idea to write

$$e^{-iH\delta_t} = e^{-\frac{i}{2}V\delta_t}e^{-iT\delta_t}e^{-\frac{i}{2}V\delta_t} + \mathcal{O}(\delta_t^3). \quad (4)$$

The exponentials of the potential are straightforward since the potential matrix is diagonal, and $e^{-iT\delta_t} = e^{-iT_x\delta_t}e^{-iT_z\delta_t}$ in the leads since $[T_x, T_z] = 0$. In the bend, $[T_\rho, T_\phi] \neq 0$, and we

use $e^{-iT\delta_t} \approx e^{-iT\rho\delta_t/2} e^{-iT_\phi\delta_t} e^{-iT\rho\delta_t/2}$.

The kinetic energy operators are evaluated as described in Appendix A and give tridiagonal matrices. Exponentiating these operators is accomplished with the Crank-Nicolson method. The time evolution is thus performed in each spatial direction separately by solving complex tri-diagonal linear equations. Each timestep requires solving a linear equation N_x times for the z' -direction, and then using the resultant Ψ and solving $2N_z + N_\phi$ linear equations for the x -direction.

The initial wavepacket is a Gaussian centered at $(x, z) = (x_0, z_0)$, with spatial widths Δ_x and Δ_z and initial average velocity v_z :

$$\Psi(x, z, t = 0) = N_0 e^{iv_z z} e^{-\frac{(x-x_0)^2}{2\Delta_x^2}} e^{-\frac{(z-z_0)^2}{2\Delta_z^2}}. \quad (5)$$

We only consider states that are in the lowest mode of the lead ($x_0 = \rho_0$ and $\Delta_x = 1$). Despite a dense transverse grid, the above analytic ground state is not exactly an eigenstate on the grid, so the normalization constant N_0 is determined numerically from a midpoint integration rule (see Appendix A). The split operator Crank-Nicolson scheme guarantees the unitarity of the wavefunction for all later times. Cigar-shaped wavepackets were employed here ($\Delta_z = 10$), which corresponds to the common experimental situation in which a BEC is prepared with transverse trapping frequencies that are significantly larger than the frequency in the direction of propagation [12, 36, 37]. They are also used since an elongated Gaussian wavepacket has a small velocity spread (in oscillator units $\Delta_z \Delta_{v_z} = 1$), reducing the effects of wavepacket dispersion. The numerical grid is large enough that the wavepacket propagates through the bend without touching the edges of the grid during the times of interest.

Expectation values were determined using a midpoint rule integration (see Appendix A). In particular, $\langle H \rangle(t) = \langle T \rangle(t) + \langle V \rangle(t)$ was monitored to ensure that the total energy variation remained at levels less than 1 part in 10^8 . To achieve such accuracy, a typical calculation (90° bend with $\rho_0 = 10$, using a wavepacket with $v_z = 3$, $\Delta_z = 10$ starting at $z_0 = -200$) required $\delta_t = 0.005$. We used $N_z = 8000$ covering $-400 < z < 0$, giving tens of points per wavelength (determined from the $\lambda = 2\pi/v_z$). In the bend, $N_\phi = 314$ points were chosen to ensure a uniform spacing along the SHO minimum in both the bend and leads. The transverse grid ensured that the oscillations of the maximum SHO mode energetically available (and a few of the closed, evanescent modes closest to threshold [26]) could be accurately described (eg. $N_x = 248$ was sufficient for $v_z = 3$).

To calculate a classical trajectory through the same bend, the Runge-Kutta method was employed to solve the classical equations of motion:

$$\frac{dp_x}{dt} = -\frac{\partial V(x, z)}{\partial x} \quad , \quad \frac{dp_z}{dt} = -\frac{\partial V(x, z)}{\partial z} . \quad (6)$$

To quantitatively compare the Ehrenfest trajectory and quantum mechanical wavepacket calculations, the transverse heating E_h is used [33]. The transverse heating measures the amount of propagation energy (E_z) transferred into transverse energy by the bend, eg. for the Ehrenfest trajectory we used

$$E_h = E_z(t \rightarrow -\infty) - E_z(t \rightarrow \infty) . \quad (7)$$

If there is no transverse energy initially — as we assume in the present calculations — E_h must be non-negative and there can be no transverse cooling. Quantum mechanically, we determined the transverse heating of a wavepacket that has been excited by the bend from the time-averages of $\langle T \rangle(t)$ and $\langle V \rangle(t)$ once the wavepacket had completely exited the bend. Further discussion of this is relegated to Appendix B.

III. RESULTS

In this section we will first discuss a series of $\phi_0 = 90^\circ$ bends with various radii ρ_0 to highlight the quantum mechanical wavepacket and Ehrenfest trajectories. We will then examine the transverse heating of both wavepackets and Ehrenfest trajectories propagating through the same bend, and compare these results with the analytic classical results of Blanchard and Zozulya [33]. The emphasis of the present calculations is on parameters close to currently realisable experimental situations, *i.e.* larger radii bends and higher propagation energies.

A. Wavepacket and Ehrenfest trajectories

The calculations in this section are presented to provide an understanding of the fundamental wavepacket and Ehrenfest trajectory dynamics. To demonstrate multimode excitation, an incoming wavepacket with $v_z = 3$ was chosen. At this energy, four excited modes are energetically open. The excitation of a wavepacket during propagation through three

different 90° bends ($\rho_0 = 15, 25, 35$) can be observed in Fig. 3, which shows the probability density $|\Psi(x, z, t)|^2$ contours of the wavepackets at three roughly equal times. In each case, a cigar-shaped wavepacket in the ground transverse state with $\Delta_z/\Delta_x = 10$ was used, and was initially located at $z_0 = -200$.

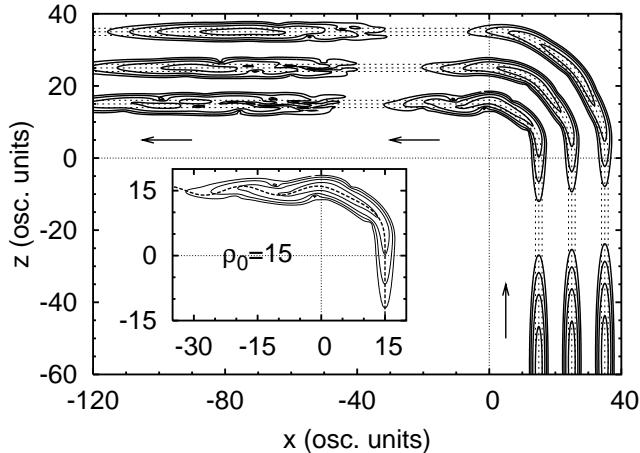


FIG. 3: Propagation of a wavepacket with $v_z = 3$ through three 90° circular bends ($\rho_0 = 15, 25, 35$) with the SHO waveguide center marked at $15 \pm 1, 25 \pm 1$ and 35 ± 1 . Three snapshots at roughly the same time are shown, with each contour line corresponding to a logarithmic decrease of $|\Psi(x, z, t)|^2$ from 10^{-2} to 10^{-5} (for the initial wavepacket, the peak probability on the grid was $|\Psi(x, z, t_0)|^2 = 3.18 \times 10^{-2}$). No reflections were observed at this level of detail. Inset: $\rho_0 = 15$ wavepacket superimposed on its Ehrenfest trajectory (dashed line).

The tightest of the three bends yields significant population of all five available modes in the final snapshot. Due to energy conservation, the conversion of longitudinal kinetic energy into transverse energy (heating) means that each excited mode has a different average propagation velocity. Consequently, the higher modes lag further and further behind the ground mode as time progresses. This effect can be seen in the final snapshots in Fig. 3, where the excited modes are showing the first signs of separating from the ground state. It should be emphasized that the number of modes available is the same for all ρ_0 shown in Fig. 3. The degree of mode-excitation, however, depends on ρ_0 . The two main conclusions of our time-independent calculations for circular waveguide bends [26] are also borne out here. That is, in general, there is minimal reflection from circular bends, and mode transfer can become significant for tight bends.

To determine the suitability of classical mechanics for this problem, we invoke Ehrenfest's theorem within the approximation shown in Eq. (1). Given the exact agreement between quantum and classical mechanics Ehrenfest's theorem usually gives for SHOs, it might well be expected that this approach would be sufficient for the present problem [38]. Ehrenfest's theorem requires that we solve the classical equations of motion with initial conditions matching the expectation values of position and velocity for the corresponding wavepacket. We thus need only consider a single classical trajectory for each wavepacket, the Ehrenfest trajectory. For the present initial wavepacket ($\Delta_x = 1$, $\Delta_z = 10$, $v_z = 3$, $x_0 = \rho_0$, $z_0 = -200$), the trajectory begins at $x_0 = \rho_0$, $z_0 \leq 0$ with $v_z = 3$, $v_x = 0$ and the resulting Ehrenfest trajectories for a series of circular 90° bends can be seen in Fig. 4. The paths of the wavepacket average position $\langle x \rangle(t)$, $\langle z \rangle(t)$ from the time-dependent quantum calculations are also shown.

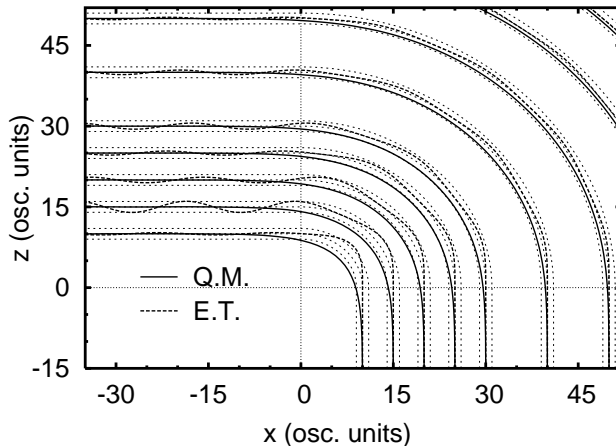


FIG. 4: Ehrenfest trajectories (E.T., dashed lines) through 90° bends for various ρ_0 , with fixed incoming velocity $v_z = 3$ (incoming from the bottom of the figure). The solid lines correspond to the path of $\langle x \rangle(t), \langle z \rangle(t)$ for the time-dependent wavepacket calculations (Q.M.). The dotted lines are the positions of the SHO minima ρ_0 and $\rho_0 \pm 1$.

The Ehrenfest trajectory *always* maintains $\rho(t) \geq \rho_0$ in the bend, even though the SHO minimum is at ρ_0 . This behavior is due to the conversion of linear momentum into angular momentum $\ell_y = v_z \rho_0$ in the bend, which results in an effective transverse potential,

$$V_{eff}(\rho) = \frac{1}{2}(\rho - \rho_0)^2 + \frac{\ell_y^2}{2\rho^2}. \quad (8)$$

Since the Ehrenfest trajectory enters with zero transverse kinetic energy, this potential has

an inner turning point at $\rho = \rho_0$ (from $V_{eff} = E_z = v_z^2/2$), and an outer turning point at $\rho = \rho_0 + 4E_z/\rho_0 + \mathcal{O}(\rho_0^{-2})$ for large ρ_0 . Thus, the Ehrenfest trajectory always exits a circular bend with $\rho \geq \rho_0$, and the outer turning point approaches $\rho = \rho_0$ for large ρ_0 . In general, this means that the amount of propagation energy transferred into transverse energy decreases with increasing ρ_0 .

In the quantum mechanical situation, the effect of the centrifugal barrier is manifested in the transverse eigenmodes within the bend: they slosh outwards with increasing energy [26]. Nevertheless, the path of a wavepacket’s average position is such that it always lies at $\langle \rho \rangle(t) \leq \rho_0$. This difference from classical mechanics stems from using an elongated initial wavepacket. For the smallest bends, the wavepacket is comparable to the bend length ($\Delta_z(t) \sim \rho_0 \phi_0$), and the difference is most exaggerated. As ρ_0 increases, with everything else held fixed, the Ehrenfest trajectories and the path of the wavepacket’s average position do approach one another at $\rho = \rho_0$ (particularly obvious in the top-right corner of Fig. 4 in the $\rho_0 = 60$ and 70 calculations).

We can see that Ehrenfest’s theorem does not give the agreement that one might expect for a SHO. This discrepancy can be understood by examining Eq. (1). For a SHO, $\langle -\partial V/\partial x \rangle = \langle -m\omega x \rangle = -m\omega \langle x \rangle$, so Ehrenfest’s theorem — and our approximation to it — is exact. A single classical trajectory will thus exactly reproduce the quantum wavepacket’s expectation values. In the present case, however, we get no such simple relation because of the bend, and must approximate $\langle -\partial V(x, z)/\partial x \rangle \approx -\partial V(\langle x \rangle, \langle z \rangle)/\partial \langle x \rangle$. This approximation makes Ehrenfest’s theorem tractable, but also leads to its eventual breakdown. Without this approximation, Ehrenfest’s theorem would be exact for all bend parameters.

Despite the discrepancy between the quantum and classical paths, a feature of these systems is best illustrated in the $\rho_0 = 15$ inset of Fig. 3, where the probability density of the wavepacket is superimposed on its Ehrenfest trajectory. This shows that, in the tight bend limit, the wiggles of a wavepacket exiting the bend do follow its Ehrenfest trajectory. The wavepacket wiggles are due to a superposition of transverse modes (see Appendix B) and, in some sense, the wiggles form the wavepacket’s “trajectory” as they are the path of maximum wavefunction flux. To further compare and contrast a wavepacket and its Ehrenfest trajectory, we next examine the amount of transverse heating by a series of circular bends.

B. Transverse Heating

The transverse heating is an experimental observable. It has been measured, for example, for a beam of cold atoms propagating through multiple circular bends [28]. Theoretically, transverse heating created by curved waveguides was investigated by Blanchard and Zozulya (BZ) [33] from a purely classical point of view. They found that transverse heating, Eq. (7), of an ensemble of classical particles on average *always* occurs as they propagate through a bend, and derived two formulas for the average transverse heating induced by a circular bend (shown in S.I. units for later comparison):

$$\langle E_h^{BZ1} \rangle = \frac{2mv_z^4}{\omega^2 \rho_0^2} \sin^2 \left(\frac{\omega \rho_0 \phi_0}{v_z} \right), \quad (9)$$

$$\langle E_h^{BZ2} \rangle = \frac{mv_z^4}{\omega^2 \rho_0^2}. \quad (10)$$

Here, $\langle E_h^{BZ1} \rangle$ assumes small longitudinal velocity spread relative to v_z , while $\langle E_h^{BZ2} \rangle$ takes into account the washing out of $\langle E_h^{BZ1} \rangle$ due to a significant spread in v_z .

The amount of transverse heating of a quantum wavepacket for a series of 90° bends with various ρ_0 and fixed initial velocity $v_z = 3$ are shown as the diamonds in Fig. 5. The transverse heating, Eq. (7), for the Ehrenfest trajectory is shown as the solid line, while three analytic results are also given: $E_h^{H.A.}$ (derived below), $\langle E_h^{BZ1} \rangle$ and $\langle E_h^{BZ2} \rangle$. The calculations shown in Figs. 3 and 4 are included, along with additional calculations to bring out the dependence on ρ_0 . There is extremely good agreement between the wavepacket and the corresponding Ehrenfest trajectory at small ρ_0 , while the present results disagree with both of the BZ formulas over the entire range of ρ_0 .

Quantum mechanically, the transverse heating of a wavepacket, *i.e.* mode-transfer, is due to the matching between the lead and bend [26] and is manifested as the excitations seen in Fig. 3. The excitation and interference of the various modes was studied in [26] as a function of ρ_0 , ϕ_0 and v_z , and is not examined here in any detail. Despite the complexity in the quantum heating mechanism, there is close agreement between the wavepacket and Ehrenfest trajectory results for small ρ_0 in Fig. 5. The small ρ_0 limit is further investigated below as a function of v_z .

At the core, the physics of transverse heating for the Ehrenfest trajectory can be understood in terms of the number of transverse oscillations that occur during propagation through the bend. Consider a harmonic approximation to the effective bend potential of

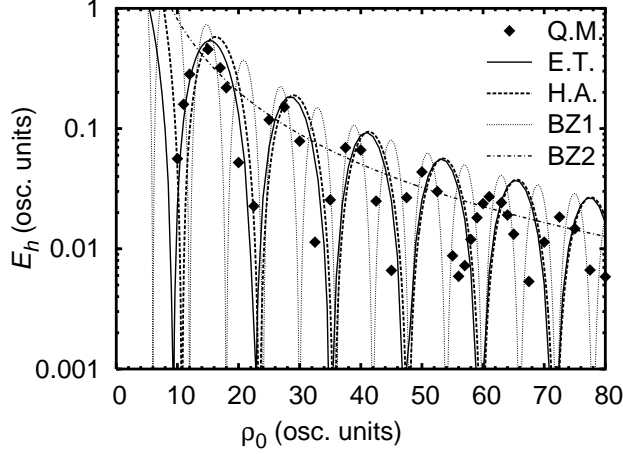


FIG. 5: Transverse heating (in oscillator units) for a 90° bend with fixed incoming $v_z = 3$ as a function of ρ_0 . The diamonds are from the time-dependent wavepacket calculations, while the Ehrenfest trajectory results form the solid line. The dashed line corresponds to an analytic result using a harmonic approximation $E_h^{H.A.}$. The dotted and dot-dashed lines correspond to the analytic results of [33], $\langle E_h^{BZ1} \rangle$ and $\langle E_h^{BZ2} \rangle$, respectively.

Eq. (8) (this section is derived in S.I. units for generality):

$$V_{eff}(\rho) \approx V(\rho_{min}) + \frac{1}{2}m\omega_{eff}^2(\rho - \rho_{min})^2, \quad (11)$$

where $\rho_{min} \approx \rho_0(1 + \alpha^2)$ and $\omega_{eff} \approx \omega(1 + \frac{3}{2}\alpha^2)$, given $\alpha = \ell_y(m\omega\rho_0^2)^{-1}$ in our approximation is small ($\alpha \ll 1$). Within the bend, the Ehrenfest trajectory thus follows

$$\frac{\rho(t)}{\rho_0} = 1 + 2\alpha^2 \sin^2 \left[\left(1 + \frac{3}{2}\alpha^2\right) \frac{\omega t}{2} \right]. \quad (12)$$

To determine the time, τ , that the particle exits the bend at $\phi(\tau) = \phi_0$ one integrates $d\phi/dt = \ell_y/(m\rho^2(t))$ using $\ell_y = mv_z\rho_0$, yielding $\tau \approx \rho_0\phi_0/v_z$. As the Ehrenfest trajectory always enters the bend with zero transverse energy, the transverse heating is determined as the transverse energy at $t = \tau$:

$$\begin{aligned} E_h^{H.A.} &= \frac{1}{2}m\dot{\rho}^2(\tau) + \frac{1}{2}m\omega^2(\rho(\tau) - \rho_0)^2 \\ &\approx \frac{2mv_z^4}{\omega^2\rho_0^2} \sin^2 \left[\left(1 + \frac{3}{2}\left(\frac{v_z}{\omega\rho_0}\right)^2\right) \frac{\omega\rho_0\phi_0}{2v_z} \right]. \end{aligned} \quad (13)$$

The agreement of $E_h^{H.A.}$ with the Runge-Kutta solution of the classical equations of motion is seen in Fig. 5 to be extremely good, although a discrepancy creeps in for small ρ_0 where the asymptotic expansion, which assumes $\alpha \ll 1$, breaks down.

The positions of the transverse heating maxima and minima for the Ehrenfest trajectory are determined by $\sin^2(\rho_0\phi_0/2v_z)$ in $E_h^{H.A.}$. When the Ehrenfest trajectory exits the bend at the outer turning point of V_{eff} the heating is a maximum *i.e.* when the parameters $\rho_0\phi_0/(2v_z) \approx (n+1/2)\pi$. Exiting at the outer turning point ensures the maximum amplitude of the transverse oscillation in the exit leads (*c.f.* Fig. 4). For the present 90° bends with fixed $v_z = 3$, the $E_h^{H.A.}$ maxima are $\rho_0 = 12$ apart, starting at $\rho_0 = 6$. The transverse heating is minimized for $\rho_0\phi_0/(2v_z) \approx n\pi$, where the trajectory exits the bend at $\rho(\tau) = \rho_0$. Of course, at $x = \rho_0$ in the exit lead there is no force acting on the Ehrenfest trajectory, and thus no transverse heating. The $E_h^{H.A.}$ transverse heating minima in Fig. 5 occur every multiple of $\rho_0 = 12$ for large ρ_0 , with a slight departure for the two minima located near $\rho_0 \approx 23$ and 10 due to the corrective term in Eq. (13).

There are two complicating factors hidden amongst the quantum and Ehrenfest comparisons: dispersion and mode-excitation. Dispersion is manifested in the wavepacket calculations as a dampening of the oscillations of E_h with ρ_0 compared to the Ehrenfest trajectory results. Mode-excitation also complicates the comparison since each mode that is excited upon entering the bend executes a different number of transverse oscillations through the bend. For $v_z = 3$, both of these velocity effects are not so significant for small ρ_0 , but begin to play a role at larger ρ_0 . While Ehrenfest's theorem is exact, the present results demonstrate that the approximation of Eq. (1) begins to breakdown in the large ρ_0 regime, where wave effects such as dispersion become significant.

The variance of the BZ results with the Ehrenfest trajectory calculations is seen in comparing Eq. (13) with Eq. (9). This clearly shows a factor of 2 difference in the sinusoidal periodicity (apart from an additional corrective term), with the $\langle E_h^{BZ1} \rangle$ formula predicting transverse heating minima at every multiple of $\rho_0 = 6$ (for 90° bends with fixed $v_z = 3$). To understand the difference in the periodicity, consider a single classical particle entering at the center of the bend with *non-zero* transverse velocity: this particle will pass through $\rho = \rho_0$ twice as it oscillates through one period of the effective potential, Eq. (8). If the exit point out of the bend occurs at $\rho(\tau) = \rho_0$, the particle exits with the same transverse speed that it entered with. This means that no transverse heating of the classical particle occurs for two points during one oscillation in the effective bend potential. In the gentle bend limit, the heating minima would indeed occur every $\rho_0 = 6$. On the other hand, the Ehrenfest trajectory, which strictly maintains $\rho(t) \geq \rho_0$ throughout the bend, requires one complete

oscillation in the bend potential to reach back to $\rho(t) = \rho_0$, (and thus heating minima occur every $\rho_0 = 12$ in the large ρ_0 limit).

The comparison of the BZ results with the quantum wavepacket calculations seen in Fig. 5 also warrants further comment. The transverse heating minima for quantum wavepackets drift away from the Ehrenfest trajectory minima as ρ_0 becomes large in Fig. 5. In this limit, it might be expected that the "gentle bend" assumption leading to Eq. (9) is better satisfied. We do not, however, observe the appearance of two minima in the quantum wavepacket calculations as per $\langle E_h^{BZ1} \rangle$. The BZ formulae are based on an analysis of an ensemble of classical particles that enter relatively gentle bends with transverse velocities much smaller than the propagation velocity. To examine the gentle bend, high velocity wavepacket limit is not only computationally taxing, but remains beyond the scope of the present paper. While the present quantum results do not agree with either of Blanchard and Zozulya's formulae, it must be emphasized that the magnitude of the five different results shown in Fig. 5 all follow the same decay trend: $E_h \propto \rho_0^{-2}$.

Finally, the dependence on velocity for a tight ($\rho_0 = 10$) bend can be seen in Fig. 6. There

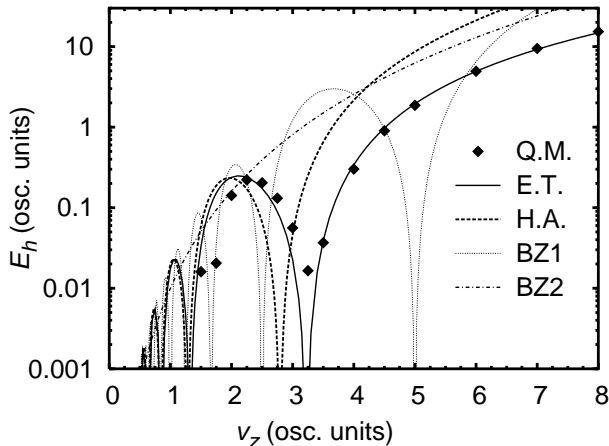


FIG. 6: Transverse heating (in oscillator units) for a 90° bend with fixed $\rho_0 = 10$ as a function of the incoming propagation velocity. The diamonds are from the time-dependent wavepacket calculations, while the Ehrenfest trajectory results form the solid line. The dashed line corresponds to an analytic result using a harmonic approximation $E_h^{H.A.}$. The dotted and dot-dashed lines correspond to the BZ analytic results, $\langle E_h^{BZ1} \rangle$ and $\langle E_h^{BZ2} \rangle$, respectively.

is striking correspondence between the transverse heating of the quantum wavepackets and

Ehrenfest trajectories for $v_z > 2$, even up to the highest energy, $v_z = 8$, where the quantum calculation has 32 energetically open modes. This agreement follows one of the fundamental postulates of quantum mechanics, Bohr's correspondence principle, which states that in the limit of high quantum number, the quantum and the classical pictures merge. This is well known for a 1-D SHO, and it is nice to see that it applies to the present potentials. The correspondence is completely lacking, of course, at low-energies since only small quantum numbers are allowed. In particular, no transverse heating of the wavepacket is allowed for $v_z \leq \sqrt{2}$ since only the ground state mode is accessible.

On the basis of the harmonic approximation in Eq. (13), the E_h minima for $\rho_0 = 10$ occur at $v_z = 2.5, 1.25$, etc. The Ehrenfest trajectory calculations deviate from this periodicity as v_z increases, since it is a tight bend in which there is a significant perturbation of the effective bend potential of Eq. (8) due to the centripetal term. The BZ formula Eq. (9) predicts additional minima at $v_z = 5, 5/3$, etc, and Fig. 6 shows a complete departure of the BZ predictions from the quantum and Ehrenfest results across the entire range of v_z . This is not unexpected since it was already seen in the $v_z = 3$, tight ρ_0 limit in Fig. 5.

IV. CONCLUSIONS

The time-dependent Schrödinger equation has been solved for non-interacting, low-energy wavepackets propagating through circular bends. Our main goal for the present time-dependent calculations was to understand the conditions under which the classical picture of atom propagation through microstructures is valid for predicting transverse excitation. To this end, a series of time-dependent quantum and Ehrenfest trajectory calculations were performed and compared.

In the tight-bend limit, $\rho_0 \leq 30$, for $v_z = 3$ there was good agreement between the transverse heating predicted by the wavepacket and the Ehrenfest trajectory calculations. In contrast to the purely SHO case, the path of the wavepacket averages $\langle x \rangle(t), \langle z \rangle(t)$ through the bend were found to be completely different from the Ehrenfest trajectory for small ρ_0 . The peak probability density of the wavepacket, however, wriggles out of the bend along the same path as the Ehrenfest trajectory. Bohr's correspondence principle is demonstrated in the tight-bend, high propagation velocity limit (where high- n modes can be excited) where great agreement is seen between the transverse heating of the wavepacket and its Ehrenfest

trajectory.

The agreement for larger ρ_0 was not as good due to the increasingly important effects of wavepacket dispersion. In general, as long as the propagation velocity is such that there are minimal wave effects (such as reflection and dispersion) the approximation to Ehrenfest's theorem introduced in Eq. (1) provides a useful approximation to the exact Ehrenfest's theorem and thus the quantum mechanics.

A note of caution should be added when extending this idea to other microstructures. For example, a wavepacket exiting an abruptly terminating transverse potential can transfer transverse energy into longitudinal energy, leading to transverse cooling [32]. In that particular study, an ensemble of classical particles was found to reproduce the wavepacket expectation values (given situations where quantum reflections did not play a role). The Ehrenfest trajectory through such a potential, however, would be completely unaffected by the changes in the transverse potentials.

As the temperature of the atoms used in atom chip experiments decreases, the modelling of experiments using Monte-Carlo simulations will increasingly need to take into account the wave nature of the atoms. The present calculations provide guidance as to when this can simply be achieved by using a single classical trajectory to calculate the quantum observables of waves propagating through simple microstructures.

Acknowledgments

This work was supported by the Department of the Navy, Office of Naval Research, and by the Research Corporation.

APPENDIX A: FINITE DIFFERENCING

Most implementations of finite differences for the Schrödinger equation implicitly require a volume element that is constant over the whole space. This condition is trivially satisfied for Cartesian coordinates and can usually be achieved through a rescaling of the wave function for other coordinate systems. Spherical coordinates are a prime example of the latter case since the radial wave function is often scaled by a factor of r to remove the first derivative from the kinetic energy, effectively putting the system into a Cartesian coordinate system

with a boundary condition.

Another common coordinate system, cylindrical coordinates, is not so easily handled — rescaling the wave function involves a factor of $\sqrt{\rho}$. The overall behavior of the wave function near $\rho=0$ is then non-analytic, making finite differencing invalid since differencing relies on Taylor series expansions. Further, straightforward differencing of the unscaled ρ equation gives a non-Hermitian operator, which is a situation to be avoided in general. The angular momentum operator in spherical coordinates suffers from similar problems upon rescaling. Somewhat *ad hoc* schemes have been formulated to deal with these problems, but are less than satisfactory from the viewpoint of wanting a general differencing scheme applicable to arbitrary coordinate systems.

One solution to this problem has actually been known for quite some time, and is based on general principles of discrete calculus and differencing [39]. Our approach is similar to Ref. [35], however, and applies the more familiar variational principle to derive the differencing equations. The derivation will be outlined for the one-dimensional time-independent equation for simplicity, but carries through in exactly the same way for the multi-dimensional time-dependent equation. We begin with the energy functional

$$E = \frac{\int \left(\frac{\hbar^2}{2\mu} \frac{d\psi^*}{dx} \frac{d\psi}{dx} + V\psi^*\psi \right) \rho(x) dx}{\int \psi^*\psi \rho(x) dx} . \quad (\text{A1})$$

Note that in writing the kinetic energy as we have will guarantee that our resulting difference representation is Hermitian. To proceed, we must choose quadrature and differencing rules for the integrals and derivatives, respectively. We choose the midpoint rule

$$\int f(x) dx \longrightarrow \sum_{i=1}^N f(x_i) (x_{i+\frac{1}{2}} - x_{i-\frac{1}{2}}) , \quad (\text{A2})$$

and central differencing

$$\left. \frac{df}{dx} \right|_{x_i} \longrightarrow \frac{f_{i+\frac{1}{2}} - f_{i-\frac{1}{2}}}{x_{i+\frac{1}{2}} - x_{i-\frac{1}{2}}} . \quad (\text{A3})$$

The grid points have been left arbitrary to allow maximum flexibility of the representation. A uniform grid can, of course, be chosen.

Substituting Eqs. (A2) and (A3) into Eq. (A1) and minimizing with respect to the wave function on the grid,

$$\frac{\partial E}{\partial \psi_j^*} = 0 , \quad (\text{A4})$$

gives the difference equation

$$\begin{aligned} \frac{\hbar^2}{2\mu} \left[\frac{\psi_j - \psi_{j-1}}{x_j - x_{j-1}} \rho_{j-\frac{1}{2}} - \frac{\psi_{j+1} - \psi_j}{x_{j+1} - x_j} \rho_{j+\frac{1}{2}} \right] \\ + V_j \psi_j \rho_j (x_{j+\frac{1}{2}} - x_{j-\frac{1}{2}}) = E \psi_j \rho_j (x_{j+\frac{1}{2}} - x_{j-\frac{1}{2}}), \end{aligned} \quad (\text{A5})$$

for $j = 1, \dots, N$. Writing this as a matrix equation,

$$\mathbf{H}\vec{\psi} = \mathbf{E}\mathbf{S}\vec{\psi}, \quad (\text{A6})$$

shows that our differencing scheme does indeed yield Hermitian operators. The Hamiltonian matrix is tridiagonal just as for the usual second-order finite differencing of the Schrödinger equation; the overlap matrix \mathbf{S} is diagonal.

This difference scheme must be supplemented by boundary conditions. If the wave function is to be zero on the boundary, then ψ_0 (or ψ_{N+1}) must be set to zero. If the derivative of the wave function is to be zero, then two grid points should be chosen to straddle the boundary point and the condition $\psi_0 = \psi_1$ imposed (or $\psi_N = \psi_{N+1}$). This condition requires that

$$\frac{\hbar^2}{2\mu} \frac{\rho_{\frac{1}{2}}}{x_1 - x_0} \quad (\text{A7})$$

be subtracted from the first diagonal element of \mathbf{H} ; a similar term should be subtracted from the last element to apply the boundary condition at the other boundary. The case in which no boundary condition is required — if $\rho=0$ — is treated the same as the zero derivative boundary condition. In all cases, the values of ρ_i outside of the grid should be chosen to be symmetric with respect to the boundary.

This equation can be put in somewhat more convenient form using the usual transformation for generalized eigenvalue problems,

$$\mathbf{S} = \mathbf{L}^T \mathbf{L}, \quad (\text{A8})$$

which is always possible for positive definite matrices \mathbf{S} . In this case, the result is trivial since \mathbf{S} is diagonal:

$$L_i = \sqrt{S_i}. \quad (\text{A9})$$

Equation (A6) can then be transformed with the relations

$$\tilde{\mathbf{H}} = \mathbf{L}^{-1} \mathbf{H} \mathbf{L}^{-T} \quad \text{and} \quad \vec{\phi} = \mathbf{L}^T \vec{\psi} \quad (\text{A10})$$

into the standard eigenvalue problem

$$\tilde{\mathbf{H}}\vec{\phi} = E\vec{\phi}. \quad (\text{A11})$$

Other transformations will produce a standard eigenvalue problem from the generalized one, but this transformation was chosen since it produces a Hermitian Hamiltonian. Explicitly, the nonzero matrix elements of $\tilde{\mathbf{H}}$ are

$$\tilde{H}_{ii} = \frac{\hbar^2}{2\mu} \left[\frac{\rho_{i-\frac{1}{2}}}{x_i - x_{i-1}} + \frac{\rho_{i+\frac{1}{2}}}{x_{i+1} - x_i} \right] \frac{1}{\rho_i(x_{i+\frac{1}{2}} - x_{i-\frac{1}{2}})} + V_i \quad (\text{A12})$$

and

$$\tilde{H}_{i,i+1} = -\frac{\hbar^2}{2\mu} \frac{\rho_{i+\frac{1}{2}}}{x_{i+1} - x_i} \times \frac{1}{\sqrt{\rho_i(x_{i+\frac{1}{2}} - x_{i-\frac{1}{2}})\rho_{i+1}(x_{i+\frac{3}{2}} - x_{i+\frac{1}{2}})}}. \quad (\text{A13})$$

The elements $\tilde{H}_{i,i-1}$ can be obtained from the symmetry of $\tilde{\mathbf{H}}$.

With our quadrature rule, normalization takes the form

$$\sum_{i=1}^N |\psi_i|^2 \rho_i(x_{i+\frac{1}{2}} - x_{i-\frac{1}{2}}) = 1. \quad (\text{A14})$$

Consequently, the transformed wave function satisfies

$$\sum_{i=1}^N |\phi_i|^2 = 1, \quad (\text{A15})$$

since the transformation includes both the volume element and step size. Care must be taken to use the physical wave function $\vec{\psi}$ for calculations or, alternatively, to derive the equivalent expressions for the transformed function $\vec{\phi}$.

The transformed Hamiltonian $\tilde{\mathbf{H}}$ and wave function $\vec{\phi}$ can be inserted directly into the Crank-Nicolson time propagation scheme in place of the usual uniform Cartesian difference Hamiltonian.

APPENDIX B: EXPECTATION VALUES FOR SHO SUPERPOSITION STATES

The time-dependence of the expectation values of time-independent operators Θ can be determined in quantum mechanics from the Heisenberg equation of motion:

$$\langle \Theta \rangle(t) = \frac{1}{i\hbar} \langle [\Theta, H] \rangle. \quad (\text{B1})$$

For energy eigenstates ψ_E , $\langle \psi_E | [\Theta, H] | \psi_E \rangle = 0$, and thus $\langle \Theta \rangle$ is time-independent. For a superposition of such states, both the time and spatial dependence of the expectation values is not so simple and is worth this brief appendix.

In our analysis, the transverse heating played the critical role in our comparisons between the quantal and classical results. The transverse heating is simply the energy transferred from the wavepackets longitudinal kinetic energy into transverse energy. Quantum mechanically, of course, we must take the expectation value of the kinetic energy operator. One might be tempted to use the virial theorem to more simply calculate this using twice the expectation value of the potential energy, however, it is well known [40] that the virial theorem only strictly holds for stationary states.

It turns out that for a simple harmonic oscillator in one dimension that the expectation value of the kinetic energy for an arbitrary state is

$$\begin{aligned} \langle \Psi | T | \Psi \rangle(t) &= \frac{1}{2} \sum_{n=0}^{\infty} \left[\left(n + \frac{1}{2}\right) |b_n|^2 \right. \\ &\quad \left. - \sqrt{(n+2)(n+1)} \operatorname{Re}(e^{2it} b_{n+2}^* b_n) \right] \end{aligned} \quad (\text{B2})$$

where b_n are the expansion coefficients of $|\Psi\rangle$ on the SHO eigenstates $|n\rangle$. The expectation value of kinetic energy thus oscillates about half the average total energy. Upon time-averaging, the second term falls out, so that the virial theorem holds on average. Since only the time-average will usually be important, this result can be handy for numerical calculations. Note that if only states with opposite parity or indices separated by more than two are populated, then the virial theorem holds for all times.

For waveguide applications such as those considered in this paper, it is convenient to write the wave function as

$$\Psi(x, z, t) = \sum_{n=0}^{\infty} \psi_n(z, t) \varphi_n(x) e^{-iE_n t} \quad (\text{B3})$$

where $\varphi_n(x)$ is the transverse SHO wave function. This multi-moded wavepacket can then be used to calculate observables. For instance, the transverse kinetic energy is

$$\begin{aligned} \langle \Psi | T_x | \Psi \rangle(t) &= \frac{1}{2} \sum_{n=0}^{\infty} \left[\left(n + \frac{1}{2}\right) \int dz |\psi_n(z, t)|^2 \right. \\ &\quad \left. - \sqrt{(n+2)(n+1)} \operatorname{Re}(e^{2it} \int dz \psi_{n+2}^*(z, t) \psi_n(z, t)) \right], \end{aligned} \quad (\text{B4})$$

and the transverse position is

$$\langle \Psi | x | \Psi \rangle(t) = \sqrt{2} \sum_{n=0}^{\infty} \sqrt{n+1} \operatorname{Re} \left(e^{it} \int dz \psi_{n+1}^*(z, t) \psi_n(z, t) \right). \quad (\text{B5})$$

So, as long as the components ψ_n overlap, they can interfere, leading to time-varying observables. As soon as the components no longer overlap — and there is no mechanism for mode conversion — the observables will become time-independent as expected.

We can also use these ideas to interpret the wave function at a fixed time by only integrating over x . The transverse position at a given time t is then

$$\langle \Psi | x | \Psi \rangle(z, t) = \sqrt{2} \sum_{n=0}^{\infty} \sqrt{n+1} \operatorname{Re} \left(e^{it} \psi_{n+1}^*(z, t) \psi_n(z, t) \right) \quad (\text{B6})$$

as a function of z . This expression can be further simplified by considering the plane-wave limit in which each component, ψ_n , has large longitudinal extent (and small spread in momentum) since we can then replace ψ_n by $b_n e^{ik_n z} e^{-i\frac{1}{2}k_n^2 t}$:

$$\langle \Psi | x | \Psi \rangle(z, t) = \sqrt{2} \sum_{n=0}^{\infty} \sqrt{n+1} \operatorname{Re} \left(b_{n+1}^* b_n e^{i(k_n - k_{n+1})z} \right) \quad (\text{B7})$$

where $k_n = \sqrt{2(E_T - n) - 1}$ and E_T is the total energy (which is the same for each mode). This time-independent expression can be used, for instance, to understand the wiggles seen in Fig. 3 as the wavepacket exits the circular bend. Where two modes overlap, the position of the resulting $\langle \Psi | x | \Psi \rangle(z)$ wiggles will be independent of time as the wavepacket propagates (like a snake threading its body through a single curved path).

Fig. 7 shows the average potential energy of wavepackets initially in the ground state of the SHO with varying incident velocity v_z as they propagate through a 90° circular bend of radius $\rho_0 = 10$. As the wavepacket is sloshing around in the bend, the potential energy increases and settles into an oscillation between kinetic and potential energies in the exit lead. As $t \rightarrow \infty$, the components ψ_n of the wavepacket will no longer overlap [see Eqs. (B4) and (B5)]. Thus, the expectation values will no longer oscillate, and the oscillations seen in Fig. 7 will dampen with time towards half of the total transverse energy. For the calculations seen here, this would involve propagating the wavepackets to stupidly large distances down the exit lead. Instead, to determine the transverse heating, we used averages of $\langle T \rangle$ and $\langle V \rangle$ over one oscillation once the wavepacket has completely exited the bend, *i.e.* the kinetic energy in the propagation direction is given by $\langle T_z \rangle = \langle T \rangle_{avg} - \langle V \rangle_{avg}$, and the transverse heating is $E_h = \langle T_z \rangle(t \rightarrow \infty) - \langle T_z \rangle(t \rightarrow -\infty)$.

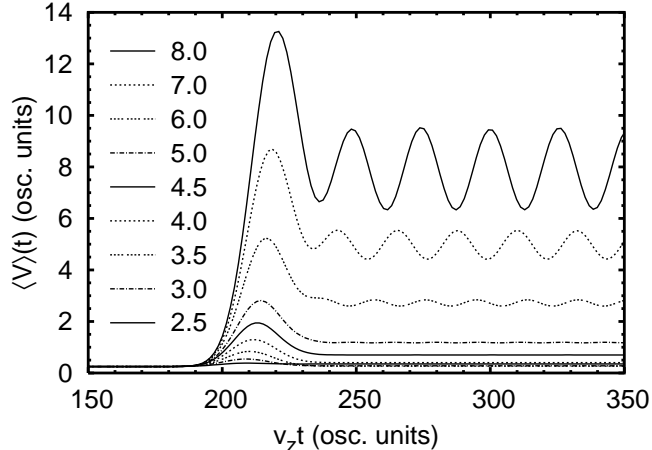


FIG. 7: $\langle V \rangle$ (in oscillator units) as a function of time for a 90° bend with fixed $\rho_0 = 10$ for incident wavepackets with varying initial velocity, v_z , ranging from 2.5 to 8.0. Each wavepacket is initially in the ground state of the SHO ($\langle V \rangle(t=0) \approx 0.25$), and transverse heating by the bend is seen as an increase in $\langle V \rangle$. The time axis has been rescaled by v_z so that the effects due to the bend (seen as the peak in $\langle V \rangle(t)$) occurs at roughly the same point in the figure.

The present Crank-Nicolson with finite difference calculations also has tiny oscillations between $\langle V \rangle$ and $\langle T \rangle$, while the total energy of the wavefunction is being conserved (typically to better 10^{-6} osc. units). These oscillations even occur during propagation through a straight SHO-based waveguide. This is due to using an initial wavepacket defined by Eq. (5) with $\Delta_x = 1$ centered at $x_0 = \rho_0$, which is not the exact eigenstate of the finite difference representation. These numerical oscillations are kept to a minimum (here less than 10^{-3} osc. units, and not visible on Fig. 7) using a dense, non-equally spaced transverse grid.

-
- [1] E. A. Hinds and I. G. Hughes, *J. Phys. D* **32**, R119 (1999).
 - [2] K. Brugger, T. Calarco, D. Cassettari, R. Folman, A. Haase, B. Hessmo, P. Krüger, T. Maier, and J. Schmiedmayer, *J. Mod. Opt.* **47**, 2789 (2000).
 - [3] J. Reichel, W. Hänsel, P. Hommelhoff, and T. W. Hänsch, *Appl. Phys. B: Lasers Opt.* **72**, 81 (2001).
 - [4] R. Folman, P. Krüger, J. Schmiedmayer, J. Denschlag, and C. Henkel, *Adv. At. Mol. Opt. Phys.* **48**, 263 (2002).

- [5] W. Hänsel, P. Hommelhoff, T. W. Hänsch, and J. Reichel, *Nature (London)* **413**, 498 (2001).
- [6] H. Ott, J. Fortagh, G. Schlotterbeck, A. Grossmann, and C. Zimmermann, *Phys. Rev. Lett.* **87**, 230401 (2001).
- [7] S. Schneider, A. Kasper, C. vom Hagen, M. Bartenstein, B. Engeser, T. Schumm, I. Bar-Joseph, R. Folman, L. Feenstra, and J. Schmiedmayer, *Phys. Rev. A* **67**, 023612 (2003).
- [8] M. P. A. Jones, C. J. Vale, D. Sahagun, B. V. Hall, and E. A. Hinds, *Phys. Rev. Lett.* **91**, 080401 (2003).
- [9] J. Reichel, W. Hänsel, and T. W. Hänsch, *Phys. Rev. Lett.* **83**, 3398 (1999).
- [10] D. M. Harber, J. M. McGuirk, J. M. Obrecht, and E. A. Cornell, *J. Low Temp. Phys.* **133**, 229 (2003).
- [11] W. Hänsel, J. Reichel, P. Hommelhoff, and T. W. Hänsch, *Phys. Rev. Lett.* **86**, 608 (2001).
- [12] A. E. Leanhardt, A. P. Chikkatur, D. Kielpinski, Y. Shin, T. L. Gustavson, W. Ketterle, and D. E. Pritchard, *Phys. Rev. Lett.* **89**, 040401 (2002).
- [13] J. Fortágh, H. Ott, S. Kraft, A. Günther, and C. Zimmermann, *Appl. Phys. B: Lasers Opt.* **76**, 157 (2003).
- [14] C. Henkel, P. Krüger, R. Folman, and J. Schmiedmayer, *Appl. Phys. B: Lasers Opt.* **76**, 173 (2003).
- [15] C. Henkel and S. A. Gardiner, e-print **cond-mat**, 0212415v2 (2003).
- [16] K. Molmer, *New J. Phys.* **5**, 55 (2003).
- [17] J. A. Stickney and A. A. Zozulya, *Phys. Rev. A* **68**, 013611 (2003).
- [18] W. Zhang, E. M. Wright, H. Pu, and P. Meystre, *Phys. Rev. A* **68**, 023605 (2003).
- [19] C. Schroll, W. Belzig, and C. Bruder, *Phys. Rev. A* **68**, 043618 (2003).
- [20] S. Chen and R. Egger, *Phys. Rev. A* **68**, 063605 (2003).
- [21] E. Andersson, T. Calarco, R. Folman, M. Andersson, B. Hessmo, and J. Schmiedmayer, *Phys. Rev. Lett.* **88**, 100401 (2002).
- [22] J. A. Stickney and A. A. Zozulya, *Phys. Rev. A* **65**, 053612 (2002).
- [23] M. D. Girardeau, K. K. Das, and E. M. Wright, *Phys. Rev. A* **66**, 023604 (2002).
- [24] M. Jääskeläinen and S. Stenholm, *Phys. Rev. A* **66**, 023608 (2002).
- [25] M. Jääskeläinen and S. Stenholm, *Phys. Rev. A* **68**, 033607 (2003).
- [26] M. W. J. Bromley and B. D. Esry, *Phys. Rev. A* **68**, 043609 (2003).
- [27] D. C. E. Bortolotti and J. L. Bohn, *Phys. Rev. A* **69**, in press (2004).

- [28] D. Müller, D. Z. Anderson, R. J. Grow, P. D. D. Schwindt, and E. A. Cornell, Phys. Rev. Lett. **83**, 5194 (1999).
- [29] J. A. Sauer, M. D. Barrett, and M. S. Chapman, Phys. Rev. Lett. **87**, 270401 (2001).
- [30] X. Luo, P. Krüger, K. Brugger, S. Wildermuth, H. Gimpel, M. W. Klein, S. Groth, R. Folman, I. Bar-Joseph, and J. Schmiedmayer, e-print **quant-ph**, 0311174 (2003).
- [31] S. Wu, W. Rooijackers, P. Striehl, and M. Prentiss, e-print **physics**, 0401123 (2004).
- [32] M. Jääskeläinen and S. Stenholm, Phys. Rev. A **66**, 053605 (2002).
- [33] N. Blanchard and A. Zozulya, Opt. Commun. **190**, 231 (2001).
- [34] J. H. Thywissen, M. Olshanii, G. Zabow, M. Drndić, K. S. Johnson, R. M. Westervelt, and M. Prentiss, Eur. Phys. J. D **7**, 361 (1999).
- [35] M. C. Witthoef, M. S. Pindzola, and J. Colgan, Phys. Rev. A **67**, 032713 (2003).
- [36] A. Kasper, S. Schneider, C. vom Hagen, M. Bartenstein, B. Engeser, T. Schumm, I. Bar-Joseph, R. Folman, L. Feenstra, and J. Schmiedmayer, J. Opt. B: Quantum Semiclassical Opt. **5**, S143 (2003).
- [37] H. Ott, J. Fortágh, S. Kraft, A. Günther, D. Komma, and C. Zimmermann, Phys. Rev. Lett. **91**, 040402 (2003).
- [38] E. A. Cornell (2003), (Priv. Comm.).
- [39] A. R. Mitchell and D. F. Griffiths, *The Finite Difference Method in Partial Differential Equations* (Wiley, New York, 1980), p. 23–26.
- [40] E. Merzbacher, *Quantum Mechanics* (Wiley, New York, U.S.A., 1970).